Title

Charge order induced Dirac pockets in the nonsymmorphic crystal TaTe4

Journal

Physical Review B, 108(15)

ISSN

2469-9950

Authors

Zhang, Yichen

Zhou, Ruixiang

Wu, Hanlin

et al.

Publication Date

2023-10-01

DOI

10.1103/physrevb.108.155121

Charge order in a nonsymmorphic topological crystal $TaTe_4$

Yichen Zhang,[1,*] Ruixiang Zhou,[2,*] Hanlin Wu,[3,*] Ji Seop Oh,[1,4] Sheng Li,[5] Jianwei Huang,[1] Jonathan D. Denlinger,[6] Makoto Hashimoto,[7] Donghui Lu,[7] Sung-Kwan Mo,[6] Kevin F. Kelly,[8] Robert J. Birgeneau,[4,9] Bing Lv,[3,†] Gang Li,[2,‡] and Ming Yi[1,§]

[1] *Department of Physics and Astronomy, Rice University, Houston, Texas, 77005 USA*
[2] *School of Physical Science and Technology, Shanghai Tech University, Shanghai 200031, China*
[3] *Department of Physics, The University of Texas at Dallas, Richardson, Texas 75080, USA*
[4] *Department of Physics, University of California, Berkeley, California 94720, USA*
[5] *School of Physics, Southeast University, Nanjing, Jiangsu 211189, China*
[6] *Advanced Light Source, Lawrence Berkeley National Laboratory, Berkeley, California 94720, USA*
[7] *Stanford Synchrotron Radiation Lightsource, SLAC National Accelerator Laboratory, Menlo Park, California 94025, USA*
[8] *Department of Electrical and Computer Engineering, Rice University, Houston, Texas, 77005, USA*
[9] *Materials Science Division, Lawrence Berkeley National Laboratory, Berkeley, California 94720, USA*

(Dated: March 28, 2023)

The interplay between charge order (CO) and nontrivial band topology has spurred tremendous interest in understanding topological excitations beyond single-particle description. In a quasi-one-dimensional nonsymmorphic crystal $TaTe_4$, the (2a×2b×3c) charged ordered ground state drives the system into a space group where the symmetry indicator features the emergence of unconventional double Dirac fermions. Using angle-resolved photoemission spectroscopy and first-principles calculations, we decipher the electronic structure of $TaTe_4$ in its CO state. We observe evidence of band folding at the Fermi level that is compatible with the new periodicity dictated by the CO, indicating that the electrons near the Fermi level follow the crystalline symmetries needed to host 8-fold fermions in this system.

I. INTRODUCTION

Since the discovery of Chern insulator and topological insulator [1–3], fascinating physics about symmetry-protected topological phases has enormously expanded the research scope of quantum materials. The idea of defining bulk topological invariants was soon extended from gapped to gapless systems, featuring Dirac and Weyl semimetals [4]. Furthermore, due to the nonsymmorphic crystalline symmetries in solid state systems, low energy electronic excitations in crystals can achieve, in addition to Dirac and Weyl fermions, unconventional 3,4,6,8-fold fermions [5–7] with no analog in the Standard Model. The experimental realization of ideal materials hosting these unconventional quasiparticles has been an ongoing task [8–19]. In particular, experimental efforts on realizing the 8-fold fermions robust against spin-orbit coupling (SOC) have been hindered by the restricted number of space groups [5] and candidates strongly affected by electron-electron (e-e) interactions [20].

Beyond pristine lattices, charge orders (CO) and charge density wave (CDW) orders can further modify the crystalline symmetries. Originating from Peierl's description of a one-dimensional (1D) chain [21, 22] where all electrons at the Fermi level (E_F) can be connected with the same vector $q = 2k_F$ (k_F being the Fermi momentum), CDW order is the spontaneous translational symmetry breaking by the electronic degree of freedom, and can arise from Fermi surface nesting (FSN), electron-phonon coupling (EPC), and e-e interaction [23], where a weak instability tendency of FSN has been pointed out beyond one dimension [24, 25]. CO shares the same phenomenology of modulated charge density upon a crystal lattice but differs in that the charge degree of freedom follows that of the lattice, which drives the translational symmetry breaking. More recently, CDWs and COs have received extensive attention due to its emergence in a series of correlated topological materials, including the possible axion physics in $(TaSe_4)_2I$ [26, 27] and the COs found in the kagome metals, both in non-magnetic AV_3Sb_5 (A = K, Rb, Cs) [28–31] and ScV_6Sn_6 [32], as well as the magnetic kagome lattice FeGe [33–35]. Therefore, investigating the interplay between CO and nontrivial topological band structure is of particular interest. Here, we focus on the scenario where the CO modifies the crystalline symmetries to produce potential unconventional topological quasiparticles, as probed in the quasi-1D material $TaTe_4$.

$TaTe_4$ crystalizes in the P4/mcc space group (#124), with Ta-chains aligned along [001] direction. $TaTe_4$ with its isostructural analogs $NbTe_4$ [38–41] and $Ta_{1-x}Nb_xTe_4$ [42–49] form to a family of quasi-1D compounds that exhibit a series of incommensurate, commensurate, and discommensurate COs. In $TaTe_4$, a (2a×2b×3c) CO has been reported by single crystal x-ray and electron diffraction experiments [38–40], with an onset temperature of $T_{CO} = 475$ K. Within the CO state, transport studies show a metallic behavior [50]. Previous ARPES measurements, however, report a sizeable gap at the Fermi level, E_F, contradictory to the metallic transport behavior [51]. Magnetotransport measurements have revealed a large magnetoresistance and quan-

tum oscillations [50, 52–55]. Nontrivial Berry phase was also suggested [53], although more rigorous analysis involving higher-order harmonics [56] may be needed to pin down the Berry phase. Furthermore, recent scanning tunneling microscopy (STM) work revealed a (4a×6c) surface CO [57] and edge states [55]. The (4a×6c) surface CO distinct from bulk was attributed to the surface-enhanced e-e interaction, with EPC stabilizing CO states at high binding energies, while the 1D edge states were proposed to be evidence of the topological nature [55] of $TaTe_4$. Regarding the bulk CO, recent first-principles calculations designated EPC the dominant role for triggering the phase transition, rather than FSN [36, 37]. Microscopically, the CO was proposed to be induced by the tendency to maximize Ta-Ta bonding, while introducing minimum shrinkage in the Te-sublattice bondings [37]. By using state-of-the-art ARPES, we study the bulk and surface electronic band structures of $TaTe_4$, which resolves previous inconsistency between ARPES spectra and optical measurements [51]. In particular, our results provide direct observation of the CO folded bands respecting the (2a×3c) periodicity near E_F — the prerequisite for the nonsymmorphic symmetry-protected multifold fermions in the CO state of $TaTe_4$. The band dispersions along high symmetry directions containing possible unconventional fermions are also investigated and compared with density functional theory (DFT) calculations. While electron correlation effects appear to be non-negligible in reconciling first-principles calculations and observations, our results provide a step towards identifying quantum materials where electronic orders can be utilized in introducing new symmetries to realize novel topological states.

II. EXPERIMENTAL METHODS

Single crystals of $TaTe_4$ were grown using flux method. High-purity Ta powder (99.99%, Alfa Asear) and Te lumps (99.9995%, Alfa Asear) with molar ratio of 1:20 were placed into a quartz tube in a glove box with O_2 level and H_2O level < 0.1 ppm. The quartz tube was flame-sealed under vacuum. The quartz tube assembly was then heated in a box furnace from room temperature up to 1000 °C in 20 hours, stayed at 1000 °C for 24 hours and then slowly cooled to 550 °C at a rate of 3°C/h. Silver needle-like crystals with a typical size of $2\times0.2\times0.2$ mm^3 were obtained by decanting the flux with a centrifuge at 550 °C using quartz wool as a filter.

Single-crystal X-ray diffraction (XRD) was performed using a Bruker SMART diffractometer equipped with an Apex II area detector, and an Oxford Cryosystems 700 Series temperature controller. A hemisphere of frames was measured using a narrow-frame method with a scan width of 0.30° in ω and an exposure time of 30 s/frame with Mo Kα radiation. The collected dataset was integrated using the Bruker Apex-II program, with the intensities corrected for the Lorentz factor, polarization, air absorption, and absorption due to variation in the path length through the detector faceplate. The data was scaled, and absorption correction was applied using SADABS [58]. A starting model was obtained using the intrinsic method in SHELXT [59], and atomic sites were refined anisotropically using SHELXL2018. Powder XRD was carried out at room temperature on a Rigaku Smartlab X-ray diffractometer with a monochromatic Cu Kα1 radiation. Electrical resistivity ρ(T,H) using four probe configuration was measured down to 2 K and up to 9 T magnetic field in a Quantum Design Physical Property Measurement System (PPMS). The composition and homogeneity of single crystals were confirmed by scanning electron microscopy with energy dispersive X-ray spectroscopy (SEM-EDX) and mapping using Zeiss EVO LS 15 SEM with 20 kV.

ARPES measurements were performed at the Advanced Light Source, Beamlines 4.0.3 and 10.0.1, equipped with SCIENTA R8000 and R4000 analyzers, respectively, and at the Stanford Synchrotron Radiation Lightsource, BL 5-2, equipped with a DA30 electron analyzer. The single crystals were cleaved *in-situ* at 10 K and measured in ultra-high vacuum with a base pressure better than 5×10^{-11} Torr. Photon energy-dependent measurements cover from 30 to 200 eV. Energy and angular resolution were set to be better than 25 meV and 0.1°, respectively.

Charge self-consistent DFT calculations were performed with the experimental lattice constants by using the generalized gradient approximation (GGA) potential [60] as implemented in Vienna *ab-initio* simulation package [61, 62]. A k-mesh of 7×7×7 for the non-CO phase and 2×2×1 for the CO phase was adopted. To better account for the interaction effect poorly approximated in GGA, we further employed the HSE06 functional to calculate the electronic structure along $\Gamma - Z$ and $X - R$ (see Fig. S5). The CO electronic structure folds back to the BZ of the non-CO state via the vaspkit code [63].

III. RESULTS AND DISCUSSION

As the crystalline symmetries are important for the topological properties, we begin by discussing the crystal structure of the pristine and CO phases. The non-CO crystal structure of $TaTe_4$ consists of tantalum chain surrounded by tellurium antiprisms (Fig. 1(a)). In the CO phase (space group P4/ncc, #130), the distorted unit cell is tripled along z and doubled along the two equivalent x and y directions (Fig. 1(b)). The lattice parameters in the CO phase identified from single crystal x-ray diffraction are: $a = b = 12.996(3)$ Å and $c = 20.385(5)$ Å (See Supplementary, Table S1). The CO introduces new

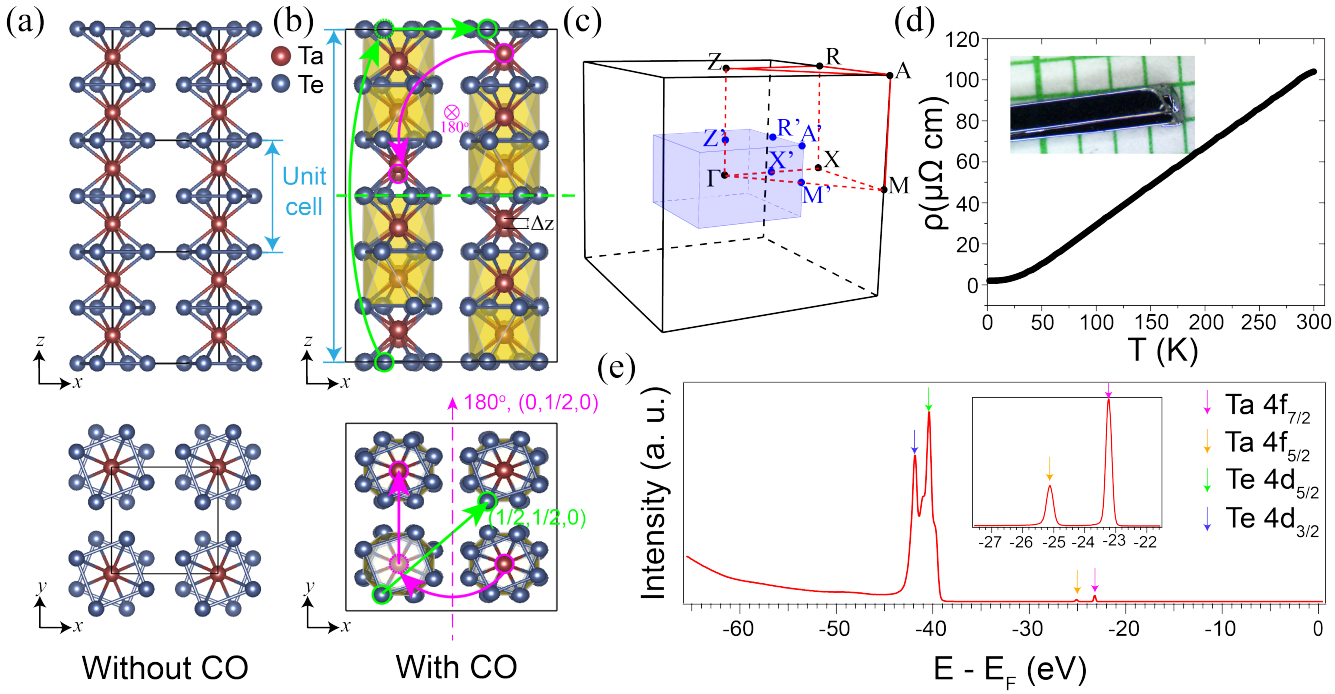

FIG. 1. Crystal structure, Brillouin zone, resistivity, and core level spectrum. (a) Side and top views of the crystal structure of $TaTe_4$ in the non-CO phase (P4/mcc, #124). x, y, and z correspond to the directions of the a, b, and c lattice vectors. (b) Same as (a) but in the CO phase (P4/ncc, #130) with a 2-fold screw axis indicated by the magenta cross pointing into the page in the side view and the magenta arrows in the top view. A glide mirror plane is indicated by a horizontal green dashed line on the side view. Magenta and green circles illustrate the transformation of atom positions after the 2-fold screw axis and glide mirror symmetry operations, respectively. The dashed magenta and green circles serve as the intermediate positions before the fractional translations. (c) Non-CO BZ (black) and CO BZ (blue) of $TaTe_4$. The folded high symmetry points are denoted in blue and with a prime on the superscript. (d) Temperature dependent resistivity data. Inset is the image of $TaTe_4$ single crystal on a millimeter-scale sheet. (e) Core level spectrum of $TaTe_4$ highlighting Ta 4f and Te 4d orbitals in colored arrows.

non-symmorphic symmetries: for example, a 2-fold screw symmetry along y and a glide mirror symmetry about the xy plane. The two symmetry operations are illustrated by the magenta and green symbols in Fig. 1(b), respectively. When transforming to the reciprocal space, the CO shrinks the pristine state BZ by a factor of (2×2×3), as depicted in Fig. 1(c). Throughout the paper, we label high symmetry points in the CO BZ in primed notation to distinguish them from their non-CO counterparts. $TaTe_4$ exhibits good metallic behavior, as indicated by the temperature-dependent resistivity with a relatively high residue resistivity ratio (RRR = 51) (Fig. 1(d)), indicating the good quality of grown single crystals. Further characterization of the single crystal magnetoresistance and homogeneity is presented in Fig. S1 and Fig. S2. In addition, core-level x-ray photoelectron spectrum identifies both Ta 4f and Te 4d peaks (Fig. 1(e)). Since the natural cleaving plane for $TaTe_4$ is the (010) plane, xz (ac) is the experimental in-plane direction, while the y direction is the out-of-plane direction in the ARPES experiments. We also note that due to the equivalence of the a and b axes of the crystal, k_x and k_y are equivalent for the bulk crystal.

We first present the overall electronic structure measured by ARPES. To determine the inner potential, we compare the k_y-k_z map measured in the out-of-plane direction by varying photon energy (Fig. 2(a)) and the equivalent k_x-k_z map measured in the in-plane direction by varying angle at the same energy (E - E_F = -0.95 eV). The bulks states should be equivalent in these two maps, while surface states would differ. From this comparison, we can identify the periodicity along k_y from a dispersive feature along Γ-X where the narrowest (widest) part is located at Γ (X), giving us an inner potential V_0 of 23 eV. From the Fermi surface (FS) measured at k_y = 0 (Fig. 2(c)), we observe rectangular pockets centered around the X points, with a periodicity compatible with the non-CO BZ, albeit strongly suppressed in the first BZ due to photoemission matrix element effects. Hence these features must be associated with the band structure of the non-CO state. We also map out dispersions along the Γ-Z and X-R directions in Fig. 2(d) and (e). Spectral intensity is dominated beyond 0.2 eV of E_F, consistent with earlier identification of the CO gap in previous ARPES results [51]. However, in contrast to earlier report where no dispersions were observed within

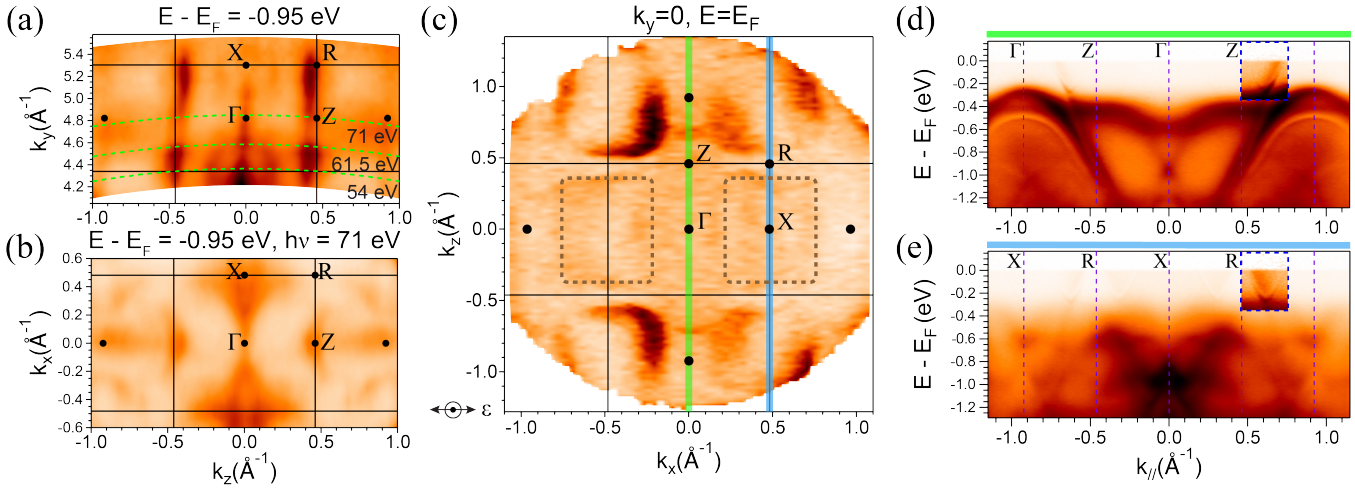

FIG. 2. Basic electronic band structure. (a) Photon-energy dependent constant energy contour at binding energy 0.95 eV where k_y corresponds to the photon energy direction. 71eV and 54eV are found out to probe $k_y = 0$ and π, respectively. (b) In-plane constant energy contour at the same binding energy as (a) to display similarities. (c) FS map using linear horizontal polarization at $k_y = 0$ plane plotted in non-CO BZ. Dashed rectangles indicate pockets that are strongly suppressed by matrix element effect in the first BZ. (d), (e) Band dispersions along Γ-Z and X-R, denoted by vertical green and blue bars in panel (c). Insets of (d) and (e) show the same region with enhanced color scale to emphasize the bands crossing the Fermi level.

the 0.2 eV gap, we clearly resolve the presence of dispersions up to E_F, reconciling the inconsistency with the metallic transport and optical conductivity behavior. From a more detailed view near E_F with an enhanced color scale, the near-E_F feature consists of a sharp outer electron pocket, with broadened intensity inside. In the following, we focus on these fine features near E_F.

To identify the bulk versus surface origin of these dispersions near E_F, we examine the photon-energy dependence measurements within 0.35 eV binding energy. We first provide a zoomed-in view of the dispersions crossing E_F probed with 54 eV (Fig. 3c). Figure 3(a) and (b) show photon-energy dependent maps at E - E_F = -40 meV and -220 meV, respectively. Notably from the X-R dispersions at E - E_F = -40 meV, the sharp and the broad electron pockets are well separated, and the intensity is dominated by the broad band near $k_{//} = \pm 0.7$ Å^{-1}, which exhibits dispersion along the out-of-plane direction, k_y (Fig. 3(a)). This indicates a bulk-nature of the broad band. At E_F = -220 meV (Fig. 3(c)), the broadened intensity vanishes, leaving behind only the sharp electron pocket bottom, which is dispersionless along k_y, consistent with a surface nature of this outer electron pocket (Fig. 3(b)). Interestingly, both the surface and bulk bands in the near-E_F region follow the periodicity of the CO BZ, as marked by the blue Γ′-Z' notation (see Fig. 3(c)). Additionally, we do not observe any evidence of the (4a×6c) surface CO suggested in recent STM work [55, 57].

To better illustrate the (2a×3c) CO folding, we performed second derivative analysis (along energy direction) on the constant energy contour at E - E_F =-0.17 eV, $h\nu = 61.5$ eV, which corresponds to the $k_y = \pi$ plane ($X'R'A'M'$ plane) for the CO BZ. On the left half of Fig. 3(d), the mirrored raw intensity of the map shows both the rectangular Fermi pockets from the non-CO BZ as marked in Fig. 2(b) as well as small elliptical pockets near the boundaries of the rectangular pockets. These small elliptical pockets can be seen more clearly in the second derivative plot on the right half of the map, where they are centered at the X' points of the (2a×3c) CO folded BZ. Examining the ellipses in greater detail, one can see the small pockets to consist of two parts: the outer surface components (white ellipses) and the inner bulk part (inner white intensities elongated along horizontal direction). Here the elliptical structure of the outer electron pockets further confirms their surface nature. Since k_x and k_y are equivalent for bulk BZ, bulk bands must show the same elliptical structure in k_x-k_z and k_y-k_z maps. However, due to the broadening effect along the out-of-plane momentum direction of the photoemission process, this would lead to broadened and filled ellipses for bulk bands (Fig. S4). In contrast, surface states are not dispersive along out-of-plane and would retain a straight feature along k_y (see Fig. S4). Next we illustrate the connection between the unfolded rectangular pockets and the folded elliptical pockets in the CO BZ (Fig. 3(e1)-(e3)). If we start with the unfolded rectangular pockets as observed in the non-CO BZ (red grids in Fig. 3(e1)-(e3)), we note that the folding of the pockets across $\boldsymbol{q}_{CDW} = (\pm\frac{1}{2}, 0, \pm\frac{1}{3})$ and its subset would indeed lead to the overlap of the rectangular pockets, as indicated by the interconnected dashed rectangles in Fig. 3(e2), the hybridization of which would

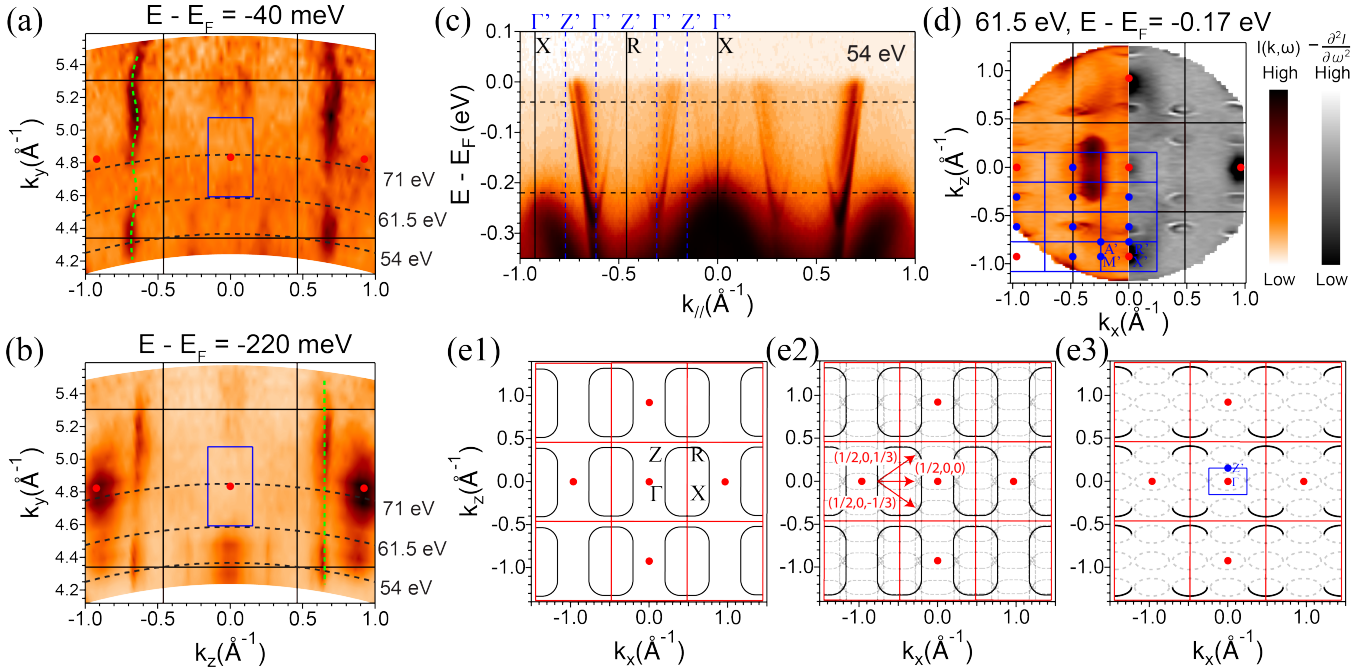

FIG. 3. CO folded bands near E_F and folding mechanism. (a), (b) Photon-energy dependent map at E - E_F = -40 and -220 meV, respectively. CO BZ is depicted by blue rectangles, while non-CO BZs are outlined in black. Green dashed curves in (a) and (b) serve as eye guidance for the warping bulk feature and non-dispersive surface feature. (c) Zoom-in on band dispersions along X-R (Γ'-Z') near E_F showing the outer surface and the inner bulk electron pockets obeying CO BZ periodicity. (d) Constant energy contour of the $X'R'A'M'$ plane at E - E_F =-0.17 eV. Raw data (from right half) mirrored to the left half and second derivative along energy for better visualization of the CO-folded pockets on the right half. (e1)-(e3) Schematic illustrations to explain the folding mechanism of the Fermi pockets. Solid and dashed transparent rectangles in (e1) and (e2) are original and folded pockets translated by $\boldsymbol{q}_{CO}$, respectively. Final folded ellipses in non-CO and CO Brillouin zones are shown in (e3).

produce elliptical pockets at the center of the CO-folded BZ, as shown in Fig. 3(e3). Here, we denote the ellipses from folding in dashed style, while the ones shared with original rectangular pockets in solid ellipses. Such band folding scheme provides a qualitative understanding of the relation between the observed unfolded rectangular pockets and the (2a×3c)-folded elliptical pockets, and confirms that the near-E_F electronic structure obeys the periodicity of the CO folding.

Since the CO introduces new nonsymmorphic symmetries to the crystal structure, we expect new topological features to arise due to the CO. In order to gain insights into the electronic structure from theory perspective, we carried out DFT calculations with different exchange-correlation functionals. In Fig. 4, we present the main results from the generalized gradient approximation (GGA) by Perdew, Burke, and Ernzerhof parameterization (PBE). First, the electronic structure of both the non-CO (Fig. 4(a)) and CO (Fig. 4(b)) states show clear metallic nature with both electron and hole pockets. The charge modulation in $TaTe_4$ does not lead to gap openings at the Fermi level, consistent with the experimental observations. As indicated by other calculations [36, 37, 55], linear band crossings exist along $\Gamma - Z$ and $M - A$ in the non-CO phase, as circled in Fig. 4(a), leading to Dirac points (DPs). The presence of the CO modifies the band topology. In addition to DPs, the CO introduces novel double Dirac points (DDPs) pinned at the A' point [5] (Fig. 4(b)). The symmetry protection mechanisms of DPs in the two phases of $TaTe_4$ are slightly different. In the non-CO phase, DPs appear along high-symmetry lines, while in the CO phase, DPs are pined at the time-reversal invariant momentum (TRIM) points.

Finally, we report on the comparison of the calculated and observed band dispersions. While some agreement can be obtained between the calculated folded bands of the CO phase with the data, such as the near-E_F electron-like dispersions along $\Gamma' - Z'$ (Fig. 4(c)), the presence of strong electron-electron correlation effects prevents a complete match of the overall electronic structure. In Fig. 4(d), we show a comparison of the experimentally observed dispersions and calculated bands for the CO backfolded to the non-CO BZ. We find that through backfolding the calculated bands from the CO to the non-CO BZ, an overall better agreement between theory and experiment can be achieved, as guided by the green dashed lines in both the ARPES and DFT panel in

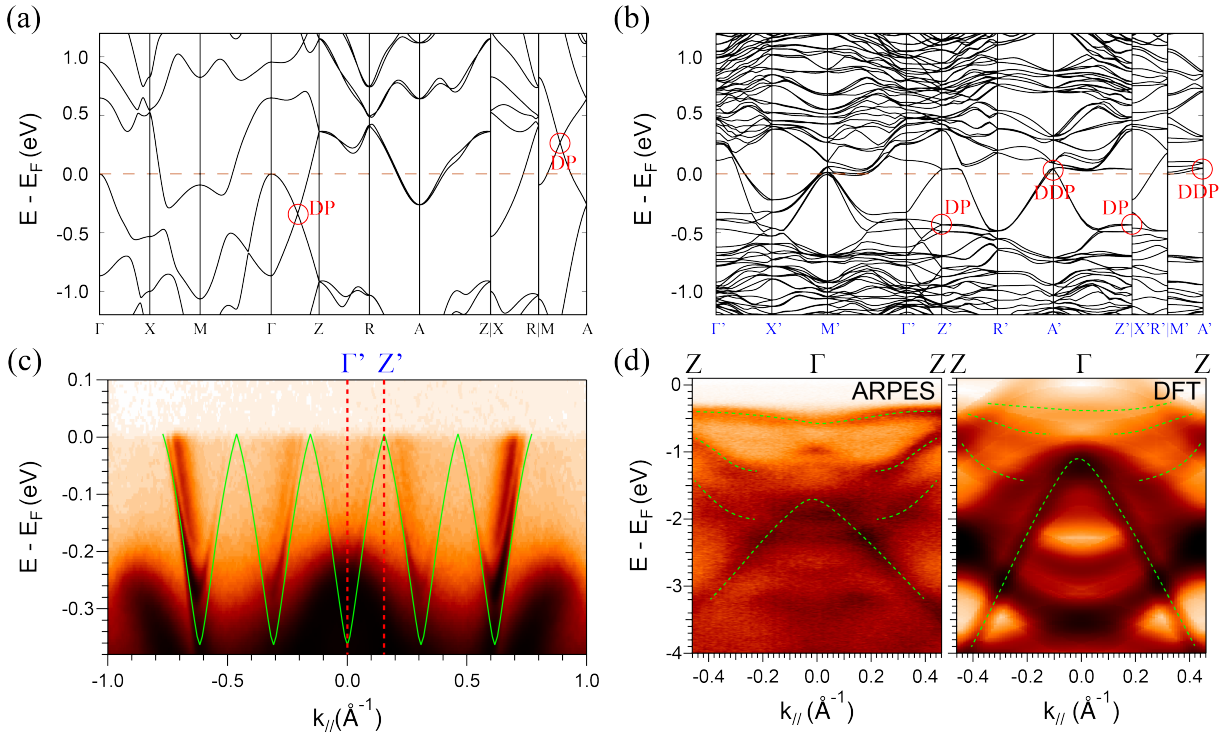

FIG. 4. ARPES spectra in comparison with DFT calculations. (a) First-principles calculations of the electronic band structure in the non-CO state with SOC. (b) Same calculation considering SOC but in the CO ground state. (c) Bulk first-principles calculations in the CO phase (green curves) overlaid on the experimental band structure for Γ'-Z' direction. (d) Comparison between backfolded first-principles calculation (right) and ARPES measured dispersions (left) along Γ-Z. Green dashed lines are to show qualitative similarities. DP: Dirac point. DDP: Double Dirac point.

Fig. 4(d). Specifically, the flat feature at around E - E_F = -0.4 eV is now qualitatively captured in the backfolding calculation, as well as the hole-like bands dispersing from E - E_F = -1 eV to -4 eV. More details of the backfolding calculation including the intensity and scattering plots are presented in Fig. S6. However, the inherent electronic correlation effects make it challenging to resolve the predicted DDPs in the CO phase (See Supplementary Information and Fig. S6). Despite the difficulty of directly observing the novel topological quasiparticles, we experimentally confirm that the low energy electronic structure follows the new symmetries of the CO phase, hence satisfying the prerequisite for hosting the symmetry-protected existence of DDPs and DPs.

IV. CONCLUSION

In summary, we have presented ARPES measurements of the electronic structure on the CO compound $TaTe_4$. We clearly reveal the presence of low energy dispersions that reconcile the inconsistency between previous ARPES report and transport results. Moreover, we directly visualize the CO-folded electron pockets with both surface and bulk components near E_F. With the folded and unfolded features disentangled in momentum space, we interpret the near-E_F electron pockets as the consequence of CO folding via the known CO wavevector $\boldsymbol{q}_{CDW} = (\frac{1}{2}, 0, \frac{1}{3})$ from original bands. Moreover, we present DFT calculations to understand the CO band structure and the role of topology in the nonsymmorphic crystal, where the DPs and DDPs are induced due to the emergent crystalline symmetries of the CO. The PBE calculations in the CO order shows partial agreement for the near-E_F electron pockets. However, discrepancies are still present between other measured bands and DFT results, implying electron correlation effects beyond the current computation machinery. Nevertheless, $TaTe_4$ presents an interesting material platform where CO induces new crystalline symmetries that result in novel topological quasiparticles in the presence of electron correlations.

ACKNOWLEDGMENTS

This research used resources of the Advanced Light Source and the Stanford Synchrotron Radiation Lightsource, both U.S. DOE Office of Science User Facilities under contract nos. DE-AC02-05CH11231 and AC02-76SF00515, respectively. ARPES work is supported by the Department of Defense, Air Force Office of Scientific

Research under Grant No. FA9550-21-1-0343, NSF under Grant Nos. DMR-1921847 and DMR-1921798. Work at University of California, Berkeley, is funded by the U.S. Department of Energy, Office of Science, Office of Basic Energy Sciences, Materials Sciences and Engineering Division under Contract No. DE-AC02-05-CH11231 (Quantum Materials program KC2202). Synthesis work at UT Dallas is by supported by NSF under Grant No. DMR-1921581 and AFOSR under grant No. FA9550-19-1-0037. Calculations were carried out at the HPC Platform of ShanghaiTech University Library and Information Services and at the School of Physical Science and Technology. G.L. acknowledges the National Natural Science Foundation of China under Grant No. 11874263, the National Key R&D Program of China under Grant No. 2017YFE0131300, and the Strategic Priority Research Program of the Chinese Academy of Sciences under Grant No. XDA18010000.

* These authors contributed equally to this work
† blv@utdallas.edu
‡ ligang@shanghaitech.edu.cn
§ mingyi@rice.edu

[1] F. D. M. Haldane, Phys. Rev. Lett. **61**, 2015-2018 (1988).
[2] C. L. Kane and E. J. Mele, Phys. Rev. Lett. **95**, 226801 (2005).
[3] C. L. Kane and E. J. Mele, Phys. Rev. Lett. **95**, 146802 (2005).
[4] N. P. Armitage, E. J. Mele and A. Vishwanath, Rev. Mod. Phys. **90**, 015001 (2018).
[5] B. J. Wieder, Y. Kim, A. M. Rappe and C. L. Kane, Phys. Rev. Lett. **116**, 186402 (2016).
[6] B. Bradlyn, J. Cano, Z. Wang, M. G. Vergniory, C. Felser, R. J. Cava and B. A. Bernevig, Science **353**, aaf5037 (2016).
[7] P. Tang, Q. Zhou and S. C. Zhang, Phys. Rev. Lett. **119**, 206402 (2017).
[8] B. Q. Lv, Z.-L. Feng, Q.-N. Xu, X. Gao, J.-Z Ma, L.-Y. Kong, P. Richard, Y.-B. Huang, V. N. Strocov, C. Fang, H.-M. Weng, Y.-G. Shi, T. Qian and H. Ding, Nature **546**, 627-631 (2017).
[9] J.-Z. Ma, J.-B. He, Y.-F. Xu, B. Q. Lv, D. Chen, W.-L. Zhu, S. Zhang, L.-Y. Kong, X. Gao, L.-Y. Rong, Y.-B. Huang, P. Richard, C.-Y. Xi, E. S. Choi, Y. Shao, Y.-L. Wang, H.-J. Gao, X. Dai, C. Fang, H.-M. Weng, G.-F. Chen, T. Qian and H. Ding, Nat. Phys. **14**, 349-354 (2018).
[10] D. Takane, Z. Wang, S. Souma, K. Nakayama, T. Nakamura, H. Oinuma, Y. Nakata, H. Iwasawa, C. Cacho, T. Kim, K. Horiba, H. Kumigashira, T. Takahashi, Y. Ando and T. Sato, Phys. Rev. Lett. **122**, 076402 (2019).
[11] H. Li, S. Xu, Z.-C. Rao, L.-Q. Zhou, Z.-J. Wang, S.-M. Zhou, S.-J. Tian, S.-Y. Gao, J.-J. Li, Y.-B. Huang, H.-C. Lei, H.-M. Weng, Y.-J. Sun, T.-L. Xia, T. Qian and H. Ding, Nat. Commun. **10**, 5505 (2019).
[12] D. S. Sanchez, I. Belopolski, T. A. Cochran, X. Xu, J.-X. Yin, G. Chang, W. Xie, K. Manna, V. Süß, C.-Y. Huang, N. Alidoust, D. Multer, S. S. Zhang, N. Shumiya, X. Wang, G.-Q. Wang, T.-R. Chang, C. Felser, S.-Y. Xu, S. Jia, H. Lin and M. Z. Hasan, Nature **567**, 500-505 (2019).
[13] N. B. M. Schröter, D.Pei, M. G. Vergniory, Y. Sun, K. Manna, F. de Juan, J. A. Krieger, V. Süss, M. Schmidt, P. Dudin, B. Bradlyn, T. K. Kim, T. Schmitt, C. Cacho, C. Felser, V. N. Strocov and Y. Chen, Nat. Phys. **15**, 759-765 (2019).
[14] N. B. M. Schröter, S. Stolz, K. Manna, F. de Juan, M. G. Vergniory,J. A. Krieger, D. Pei, T. Schmitt, P. Dudin, T. K. Kim, C. Cacho,B. Bradlyn, H. Borrmann, M. Schmidt, R. Widmer, V. N. Strocov and C. Felser, Science **369**, 179-183 (2020).
[15] B. Q. Lv, Z.-L. Feng, J.-Z. Zhao, Noah F. Q. Yuan, A. Zong, K. F. Luo, R. Yu, Y.-B. Huang, V. N. Strocov, A. Chikina, A. A. Soluyanov, N. Gedik, Y.-G. Shi, T. Qian and H. Ding, Phys. Rev. B **99**, 241104(R) (2019).
[16] X. Yang, T. A. Cochran, R. Chapai, D. Tristant, J.-X. Yin, I. Belopolski, Z. Cheng, D. Multer, S. S. Zhang, N. Shumiya, M.Litskevich, Y. Jiang, G. Chang, Q. Zhang, I. Vekhter, W. A. Shelton, R. Jin, S.-Y. Xu and M. Z. Hasan, Phys. Rev. B **101**, 201105 (2020).
[17] N. Kumar, M. Yao, J. Nayak, M. G. Vergniory, J. Bannies, Z. Wang, N. B. M. Schröter, V. N. Strocov, L. Müchler, W. Shi, E. D. L. Rienks, J. L. Mañes, C. Shekhar, S. S. P. Parkin, J. Fink, G. H. Fecher, Y. Sun, B. A. Bernevig and C. Felser, Adv. Mater. **32**, 1906046 (2020).
[18] W. Ju, J.Jeong, E.-J. Cho, H.-J. Noh, K. Kim and B.-G. Park, Phys. Rev. B. **106**, 205125 (2022).
[19] H. Rong, Z. Huang, X. Zhang, S. Kumar, F.Zhang, C. Zhang, Y. Wang, Z. Hao, Y. Cai, L. Wang, C. Liu, X.-M. Ma, S. Guo, B. Shen, Y. Liu, S. Cui, K. Shimada, Q. Wu, J. Lin, Y. Yao, Z. Wang, H. Xu and C. Chen, arXiv. 2208. 029672 (2022).
[20] D. D. Sante, A. Hausoel, P. Barone, J. M. Tomczak, G. Sangiovanni, and R. Thomale, Phys. Rev. B. **96**, 121106(R) (2017).
[21] R. E. Peierls, *Quantum theory of solids* (Oxford Univ. Press, Oxford, 1955).
[22] H. Fröhlich, Proc. R. Soc. Lond. A. **223**, 296-305 (1954).
[23] X. Zhu, Y. Cao, J. Zhang, E. W. Plummer, and J. Guo, Proc. Natl. Acad. Sci. U. S. A. **112**, 2367-2371 (2015).
[24] M. D. Johannes and I. I. Mazin, Phys. Rev. B **77**, 165135 (2008).
[25] X. Zhu, J. Guo, J. Zhang, and E. W. Plummer, Adv. Phys. X. **2**, 622-640 (2017).
[26] J. Gooth, B. Bradlyn, S. Honnali, C. Schindler, N. Kumar, J. Noky, Y. Qi, C. Shekhar, Y. Sun, Z. Wang, B. A. Bernevig and C. Felser, Nature **575**, 315-319 (2019).
[27] W. Shi, B. J. Wieder, H. L. Meyerheim, Y. Sun, Y. Zhang, Y. Li, L. Shen, Y. Qi, L. Yang, J. Jena, P. Werner, K. Koepernik, S. Parkin, Y. Chen, C. Felser, B. A. Bernevig and Z. Wang, Nat. Phys. **17**, 381-387 (2021).
[28] H. Li, T. T. Zhang, T. Yilmaz, Y. Y. Pai, C. E. Marvinney, A. Said, Q. W. Yin, C. S. Gong, Z. J. Tu, E. Vescovo, C. S. Nelson, R. G. Moore, S. Murakami, H. C. Lei, H. N. Lee, B. J. Lawrie, and H. Miao Phys. Rev. X. **11**, 031050 (2020).
[29] S. Wu, B. R. Ortiz, H. Tan, S. D. Wilson, B. Yan, T. Birol, and G. Blumberg, Phys. Rev. B. **105**, 155106 (2022).

[30] H. Luo, Q. Gao, H. Liu, Y. Gu, D. Wu, C. Yi, J. Jia, S. Wu, X. Luo, Y. Xu, L. Zhao, Q. Wang, H. Mao, G. Liu, Z. Zhu, Y. Shi, K. Jiang, J. Hu, Z. Xu, and X. J. Zhou, Nat. Commun. **13**, 273 (2022).

[31] Y. Xie, Y. Li, P. Bourges, A. Ivanov, Z. Ye, J.-X. Yin, M. Z. Hasan, A. Luo, Y. Yao, Z. Wang, G. Xu, and P. Dai, Phys. Rev. B. **105**, L140501 (2022).

[32] S. Cheng, Z. Ren, H. Li, J. Oh, H. Tan, G. Pokharel, J. M. DeStefano, E. Rosenberg, Y. Guo, Y. Zhang, Z. Yue, Y. Lee, S. Gorovikov, M. Zonno, M. Hashimoto, D. Lu, L. Ke, F.Mazzola, J. Kono, R. J. Birgeneau, J.-H. Chu, S. D. Wilson, Z. Wang, B. Yan, M. Yi, I. Zeljkovic, arXiv. 2302. 12227 (2023).

[33] X. Teng, L. Chen, F. Ye, E. Rosenberg, Z. Liu, J.-X. Yin, Y.-X. Jiang, J. S. Oh, M. Z. Hasan, K. J. Neubauer, B. Gao, Y. Xie, M. Hashimoto, D. Lu, C. Jozwiak, A. Bostwick, E. Rotenberg, R. J. Birgeneau, J.-H. Chu, M. Yi and P. Dai, Nature **609**, 490-495 (2022).

[34] X. Teng, J. S. Oh, H. Tan, L. Chen, J. Huang, B. Gao, J.-X. Yin, J.-H. Chu, M. Hashimoto, D. Lu, C. Jozwiak, A. Bostwick, E. Rotenberg, G. E. Granroth, B. Yan, R. J. Birgeneau, P. Dai, M. Yi, arXiv. 2210. 06653 (2022).

[35] J.-X. Yin, Y.-X. Jiang, X. Teng, Md. S. Hossain, S. Mardanya, T.-R. Chang, Z. Ye, G. Xu, M. M. Denner, T. Neupert, B. Lienhard, H.-B. Deng, C. Setty, Q. Si, G. Chang, Z. Guguchia, B. Gao, N. Shumiya, Q. Zhang, T. A. Cochran, D. Multer, M. Yi, P. Dai, and M. Z. Hasan, Phys. Rev. Lett. **129**, 166401 (2022).

[36] F.-H. Liu, W. Fu, Y.-H. Deng, Z.-B. Yuan, and L.-N. Wu, Appl. Phys. Lett. **119**, 091901 (2021).

[37] B. Guster, M. Pruneda, P. Ordejón, and E. Canadell, Phys. Rev. B. **105**, 064107 (2022).

[38] E. Bjerkelund and A. Kjekshus, J. Less-Common Met. **7**, 231 (1964).

[39] F. W. Boswell, A. Prodan and J. K. Brandon, J. Phys. C: Solid State Phys. **16**, 1067-1076 (1983).

[40] J. Mahy, J. Van Landuyt and S. Amelinckx, Phys. Status Solidi (a) **77**, K1-K4 (1983).

[41] K. Selte and A. Kjekshus, Acta Chem. Scand. **18**, 690-696 (1964).

[42] D. J. Eaglesham, D. Bird, R. L. Withers and J. W. Steeds, J. Phys. C: Solid State Phys. **18**, 1-11 (1985).

[43] R. Morelli, D. Sahu, and M. B. Walker, Phys. Rev. B. **33**, 4843-4848 (1986).

[44] F. W. Boswell and A. Prodan, Phys. Rev. B. **34**, 2979(R) (1986).

[45] M. B. Walker and R. Morelli, Phys. Rev. B. **38**, 4836 (1988).

[46] A. Prodan, F. W. Boswell, J. C. Bennett, J. M. Corbett, T. Vidmar, V. Marinkovic and A. Budkowski, Acta Crystallogr. Sect. B **46**, 587-591 (1990).

[47] J. C. Bennett, S. Ritchie, A. Prodan, F. W. Boswell and J. M. Corbett, J. Phys.: Condens. Matter **4**, 2155 (1992).

[48] J. Kusz and H. Böhm, Acta Crystallogr. Sect. B **50**, 649-655 (1994).

[49] J. Kusz, H. Böhm and J. C. Bennett, J. Phys.: Condens. Matter **7**, 2775-2782 (1995).

[50] S. Tadaki, N. Hino, T. Sambongi, K. Nomura, F. Lévy, Synth. Met. **38**, 227-234 (1990).

[51] F. Zwick, H. Berger, M. Grioni, G. Margaritondo, L. Forró, J. LaVeigne, D. B. Tanner, and M. Onellion, Phys. Rev. B. **59**, 7762 (1999).

[52] T. Sambongi, S. Tadaki, N. Hino, and K. Nomura, Synth. Met. **58**, 109-114 (1993).

[53] X. Luo, F. C. Chen, Q. L. Pei, J. J. Gao, J. Yan, W. J. Lu, P. Tong, Y. Y. Han, W. H. Song, and Y. P. Sun, Appl. Phys. Lett. **110**, 092401 (2017).

[54] Y. Gao, L. Xu, Y. Qiu, Z. Tian, S. Yuan, and J. Wang, J. Appl. Phys. **122**, 135101 (2017).

[55] X. Zhang, Q. Gu, H. Sun, T. Luo, Y. Liu, Y. Chen, Z. Shao, Z. Zhang, S. Li, Y. Sun, Y. Li, X. Li, S. Xue, J. Ge, Y. Xing, R. Comin, Z. Zhu, P.Gao, B. Yan, J. Feng, M. Pan, and J.Wang, Phys. Rev. B. **102**, 035125 (2020).

[56] A. Alexandradinata, C. Wang, W. Duan, and L. Glazman, Phys. Rev. X. **8**, 011027 (2018).

[57] H. Sun, Z. Shao, T. Luo, Q. Gu, Z. Zhang, S. Li, L. Liu, H. Gedeon, X. Zhang, Q. Bian, New J. Phys. **22**, 083025 (2020).

[58] L. Krause, R. Herbst-Irmer, G. M. Sheldrick, and D. Stalke, J. Appl. Crystallogr. **48**, 3-10 (2015).

[59] G. M. Sheldrick, Acta Crystallogr. Sect. C Struct. Chem. **71**, 3-8 (2015).

[60] J. P. Perdew, K. Burke, and M. Ernzerhof, Phys. Rev. B. **77**, 3865 (1996).

[61] G. Kresse and J. Furthmüller, Phys. Rev. B. **54**, 11169 (1996).

[62] G. Kresse and J. Furthmüller, Comput. Mater. Sci. **6**, 15-50 (1996).

[63] V. Wang, N. Xu, J.-C. Liu, G. Tang, W.-T. Geng, Comput. Phys. Commun. **267**, 108033 (2021).